quaternary

MDPI

Article

Evidence for an Extreme Cooling Event Prior to the Laschamp Geomagnetic Excursion in Eifel Maar Sediments

Johannes Albert * and Frank Sirocko

Department for Geoscience, Johannes-Gutenberg University, 55128 Mainz, Rhineland-Palatinate, Germany
* Correspondence: jalber01@uni-mainz.de

Abstract: We present a timeseries of flood and slumping phases in central Europe for the past 65,000 years from event layers in sediment cores from infilled Eifel maar basins (Germany). Palynological, petrographic and organic carbon (chlorins) records are used to understand the precise timing of these events. Periods of increased flood activity seem to coincide with Heinrich stadials in marine sediment records, which are associated with cold and more arid climate conditions, indicating a vegetation response within the maars' catchment areas. This multi-proxy correlation reveals prominent slumps at different maar sites during Greenland Stadial (GS) 12. The stratigraphy is based on sediment records from the Auel infilled maar and we thus call this event Auel Cold Event (ACE). Frozen and fractured sediment packages within the slump suggest deep frost or permafrost conditions for the region during the stadial. The results agree well with sediment archives and archeological sites across Europe that report severely cold and arid conditions for the stadial. This supports the assumption that GS12 was indeed one of the coldest periods of the last glacial cycle rather than the Heinrich stadials. Based on our age model, the ACE occurred at 43,500 yr b2k (years before the year 2000), which coincides with the initial weakening of Earth's magnetic field strength prior to the Laschamp geomagnetic excursion.

Keywords: Eifel; maar sediments; flood frequency; slumping events; permafrost; Greenland Stadial 12; Laschamp geomagnetic event; Heinrich stadials

Citation: Albert, J.; Sirocko, F. Evidence for an Extreme Cooling Event Prior to the Laschamp Geomagnetic Excursion in Eifel Maar Sediments. *Quaternary* **2023**, *6*, 14. https://doi.org/10.3390/quat6010014

Academic Editor: Matthew Peros

Received: 28 September 2022
Revised: 10 December 2022
Accepted: 30 January 2023
Published: 12 February 2023

1. Introduction

During the last glacial cycle, the northern hemisphere underwent a series of climate fluctuations. Cold and arid stadials were interposed with warm and humid interstadials. Because it was first observed in Greenland ice cores, this succession is known as Greenland Stadials (GS) and Greenland Interstadials (GI) [1–3]. During interstadial periods, prominent decadal-scale climate variations prevailed in central Europe [4]. However, these climate oscillations were essentially muted during stadial phases due to a North Atlantic sea-ice expansion and a weakening of the Atlantic Meridional Overturning Circulation. While steppe biomes were wide-spread in Europe during stadial periods, forests evolved during interstadials [5]. Throughout early Marine Isotope Stage (MIS) 3 (60,000–49,000 yr b2k (years before the year 2000)), a spruce-dominated warm temperate mixed forest with hornbeams and other thermophilous tree taxa was present in the Eifel region [6,7]. This lush forest receded near the end of GI13 and cold temperate forests expanded during subsequent stadials. The landscape further evolved at the end of GI8 (36,500 yr b2k) into a forest-steppe with scattered birch and pine trees, into a forest-tundra environment with abundant Ranunculaceae 28,500 yr b2k ago, and finally at 23,000 yr b2k into the polar desert of the Last Glacial Maximum (LGM) [6,7].

The stadial/interstadial succession was accompanied by repeated volcanic activity across the Eifel which caused the formation of numerous maar lakes in the region and the deposition of distinctive tephra layers in their sediments (e.g., [8–10]). The ELSA (Eifel Laminated Sediment Archive) project at the University of Mainz has systematically drilled

and studied more than 50 sediment cores from the open maar lakes and Pleistocene infilled maar structures of the West Eifel Volcanic Field (e.g., [7,11–14]). The near annual-resolution ELSA-20 climate proxy record shows striking structural similarities to the NGRIP $\delta^{18}O$ ice core chronology [2], showing a complete succession back to GI17 [4]. The ELSA-Flood-Stack [15] reconstructs main flood phases in the Eifel for the past 60,000 years and the ELSA-Tephra-Stack [9,10] contains the region's volcanic history from the Laacher See volcanic eruption around 13,000 years ago [16,17] back to 500,000 years.

Here, we present timeseries of flooding and slumping events covering the past 65,000 years from several Eifel maar lakes based on palynological, petrographic and organic carbon (chlorins) records. The stratigraphic foundation of this multi-proxy, multi-core correlation is the near annual ELSA-20 record [4], which allows for a high-resolution study of the timings of flood and slumping phases in the region.

2. Materials and Methods

2.1. Coring Sites

Lacustrine basins that allow climate reconstructions beyond the Holocene era are scarce in Europe and limited to a few regions (e.g., [18,19]). One of these regions is the Eifel, located in a homogenous climate zone that stretches across central Europe [20]. This study includes sediment records from the Pleistocene maar basins of Auel Maar, Dehner Maar, Merscheider Maar, Oberwinkler Maar and Rother Maar (Figures 1 and S1). Cores have been recovered using 'Seilkern' coring technology. A detailed overview for all coring sites is given in Table 1.

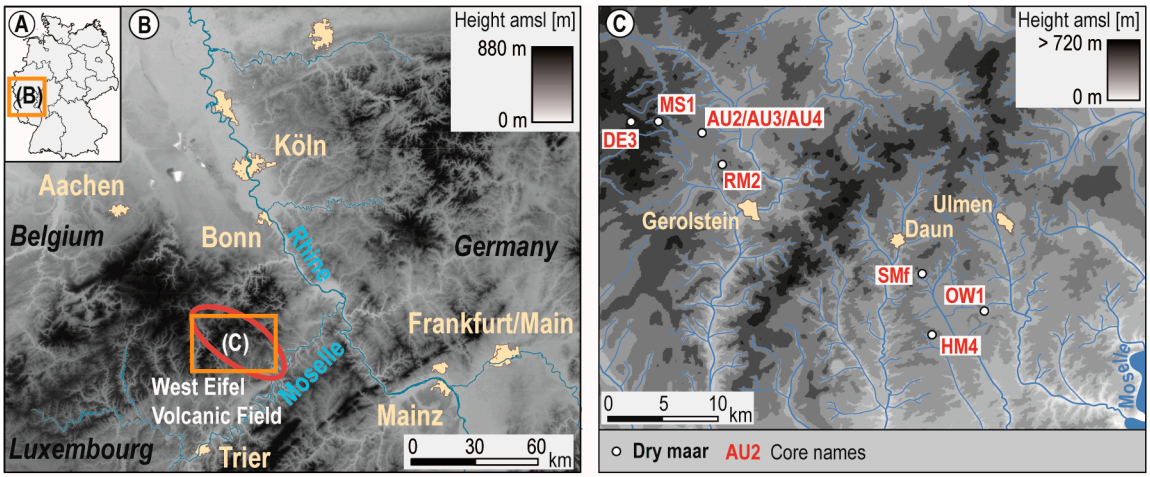

Figure 1. Location of coring sites. (**A**) Overview of Germany. Digital elevation maps of (**B**) West Germany with the West Eifel Volcanic Field (red outline) and (**C**) the West Eifel Volcanic Field with drainage system and maar locations (after [8]).

The Auel infilled maar with a diameter of 1325 m is one of the larger maar structures of the Eifel [15,21]. Today, the Tieferbach, which has a catchment area of 12,187 km^2, flows through its former center from west to east. Cores AU2, AU3 and AU4 have respective lengths of 123 m, 102 m and 104.5 m (Figures S2–S4). Of these, AU2 and AU4 reach well into the maar's eruption sequence. Due to its abundant fluvial input, the Auel cores have the highest average sedimentation rate (2 mm/year) of all ELSA cores and AU3 and AU4 were used for the near annual-resolution C_{org}(chlorins) record presented by Sirocko et al. [4].

The Dehner Maar with a diameter of 950 m and a near circular basin is still very recognizable in the landscape. Although there are no traces of a past inflow, there is an outflow to the west [13]. Core DE3 is 88 m long and reaches the basis of the lake sediments (Figure S5). The sediment record shows annual layer preservations over large parts and is therefore varve counted from the Laacher See tephra layer (13,056 yr b2k) [17] back to 26,770 yr b2k, almost reaching GI3 [6].

Table 1. Overview of coring sites included in this study.

Maar Lake	Diameter [m]	Core	Height above Sea Level [m]	Time Span Coverage [yr b2k]	Core Depth [m]	UTM Coordinates
Auel Maar	1293	AU2	452.90	10,000–59,130	123.0	32 N 328,668.00 5,572,850.00
		AU3	452.40	10,000–59,120	102.0	32 N 328,686.00 5,572,859.00
		AU4	451.50	10,000–59,130	104.5	32 N 328,732.00 5,572,977.00
Dehner Maar	931	DE3	565.37	12,000–76,250	88.0	32 N 322,384.42 5,574,206.47
Mehrscheider Maar	771	MS1	528.00	28,600–65,700	69.0	32 N 324,823.03 5,574,125.16
Oberwinkler Maar	800	OW1	385.00	25,800–72,000	49.0	32 N 352,719.74 5,556,393.10
Rother Maar	823	RM2	453.00	7700–66,400	65.0	32 N 330,075.77 5,570,533.04

The Merscheider Maar and the Rother Maar have diameters of 771 m and 823 m, respectively [21]. Today, the Mannebacher creek (Merscheider Maar—catchment area of 1.78 km^2) and the Rother creek (Rother Maar—catchment area of 2.33 km^2) flow through the former maar basins. The 69 m (MS1) and 65 m (RM2) long sediment records, which were drilled near the maars' centres, both reach into their respective eruption sequence (Figures S6 and S7).

Located approximately 25 km southeast of the other maars (Figure 1), the Oberwinkler Maar has a diameter of around 800 m [21] and is embedded in a smooth valley with two small creeks flowing through its basin. Core OW1 has a length of 48 m (Figure S8) and, although it does not reach the basis of the lake sediments, it extends into MIS 4 [22].

2.2. The ELSA-20 Stratigraphy

The ELSA-20 chronology [4] consists of sediment records from the Pleistocene maar basin of Auel (AU3 and AU4) and the Holocene maar lakes of Schalkenmehren (SMf) and Holzmaar (HM4), which are located near the Oberwinkler Maar approximately 25 km southeast of Auel (Figures 1 and 2).

To decrease the number of gaps in the Auel record, AU3 and AU4 were cored with an offset of 0.5 m and drilling positions were only 5 m apart [4]. A dynamic time warp algorithm was applied to the organic carbon (chlorins) data of both cores to determine structural similarities (Figure 2A,B). Gaps in the AU4 data were then filled with available data points in the AU3 core's corresponding segments. In the resulting AUcomp record (Figure 2C), events such as tephra layers, slumps and drilling artefacts were given zero time in the age/depth model. Slumps and drilling artefacts were determined visually on the sediment cores, while tephra layers were identified by their petrographic composition [9]. The result is the ELSA-20 climate proxy record (Figure 2D), which was then age-tuned to the stadial/interstadial succession of the NGRIP ice cores (Figure 2E) [2] using a Bayesian age model.

2.3. Tephrochronology

Most discrete tephra layers are characterized by distinct coarser grained, greyish to black event deposits in contrast to the yellowish to brown finer-grained background sediments. The volcanic layer succession in the Eifel cores was sampled and processed by Förster and Sirocko [9] and Förster et al. [10]. Six known tephra layers were identified based on their specific petrographic signature in the sediments of the five presented sites (Table 2; Figures 3, 4 and S1), i.e., the Laacher See Tephra (LST—13,056 yr b2k) [17], the Eltville Tephra (EVT—24,720 yr b2k), the Wartgesberg Tephra (WBT—28,100 yr b2k), the Dreiser Weiher Tephra (DWT—40,370 yr b2k), the Meerfelder Maar Tephra (MMT—47,340 yr b2k) and the Auel Maar Tephra (AUT—59,130 yr b2k). Furthermore, one tephra of unknown origin (UT1 [Unknown Tephra 1]—30,300 yr b2k) was found in the sediments. Accordingly, deposits of the Laacher See and Eltville eruptions were deposited in the Auel Maar and Dehner Maar. The WBT and the UT1 are visible in the Auel Maar, Dehner Maar and Rother

Maar. The UT1 was additionally found in core MS1. The DWT was deposited in the Auel Maar, Merscheider Maar and Rother Maar. The MMT is visible in all presented cores as well as the AUT, except core AU3, which does not reach down to the eruption sequence. Volcanic eruptions were used to correlate the presented sediment records using tephra layers as anchor points (Figures 3 and 4). Age of the EVT derives from varve counting done on core DE3 [6]. Ages of all other marker tephra layers except LST are based on the ELSA-20 stratigraphy (Figure 2) [4].

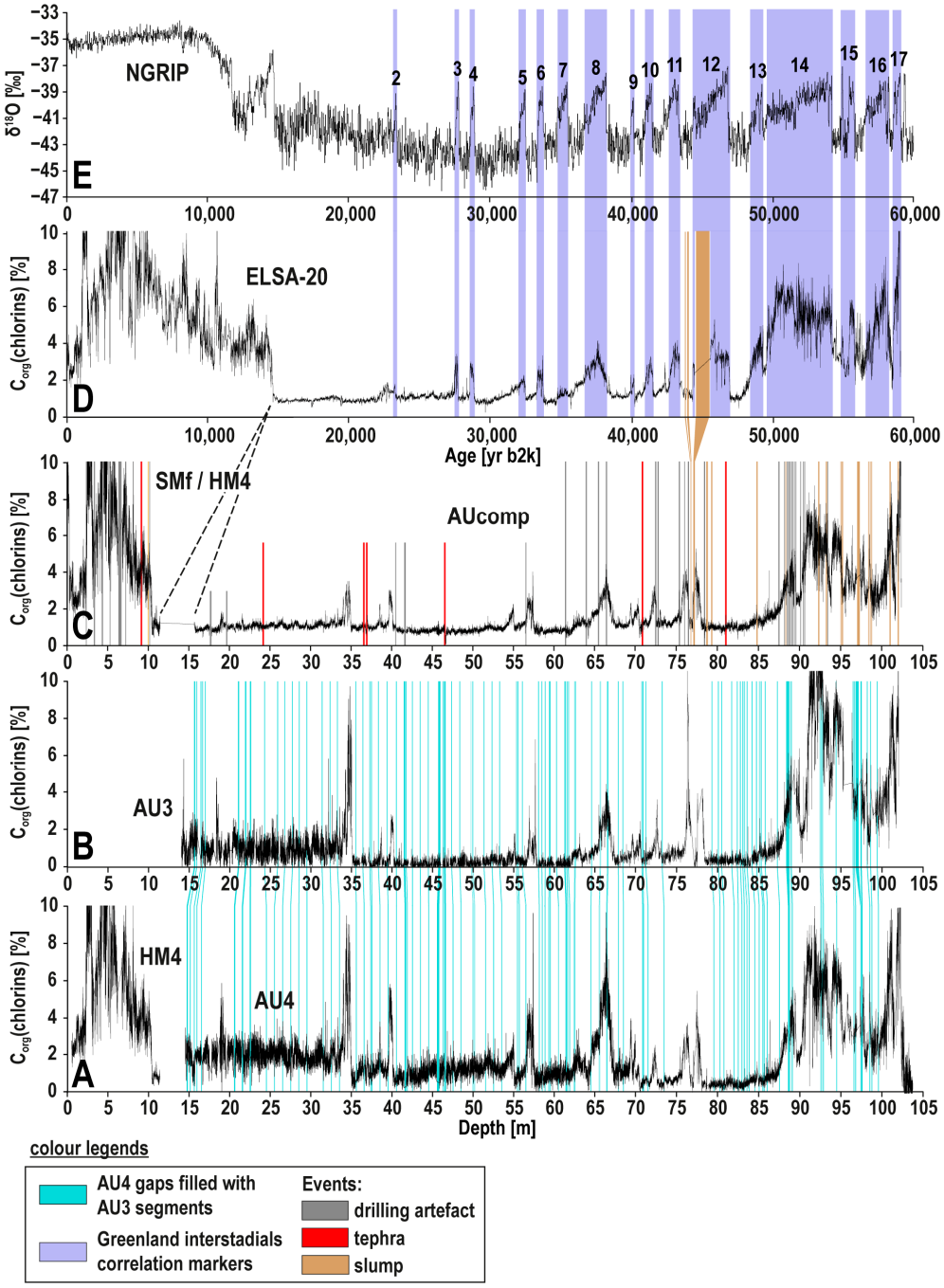

Figure 2. The ELSA-20 stratigraphy. C_{org}(chlorins) data of cores (**A**) AU4 and HM4 and (**B**) AU3. Gaps in AU4 data were filled with available data points in AU3 corresponding segments. (**C**) In the resulting AUcomp dataset, events such as tephra layers, slumps and drilling artefacts were given a time period of formation equal to zero. (**D**) The result is the ELSA-20 climate proxy record [4], which was then age-tuned to (**E**) Greenland Interstadials (GI) 2–17 of the NGRIP ice cores [2].

Table 2. Stratigraphic tie-points of presented cores. Core depths of tie-points to the NGRIP Greenland Interstadial (GI) succession [2] are listed in cores' respective columns. Highlighted are identified marker tephra layers (red) and the Auel Cold Event (ACE—grey), a massive slumping event during GS12. Age of the EVT derives from varve counting done on core DE3 [6]. Ages of all other marker tephra layers except LST [17] are based on the ELSA-20 stratigraphy [4]. Listed depths of cores AU3 and AU4 are according to Sirocko et al. [4]. Additionally, Landscape Evolution zones (LEZ) 3–8 [6,7] and their characteristic landscapes are shown.

LEZ	Time Marker	Age [yr b2k]	AU2 [m]	AU3 [m]	AU4 [m]	DE3 [m]	MS1 [m]	OW1 [m]	RM2 [m]
LEZ 3	LST top		13.80	13.59	14.40	3.40			
Cold, temperate	LST base	13,056	13.95	13.69	14.50	3.48			
forest	Onset GI1	14,692	14.65	14.68	15.61	10.00			7.70
LEZ 4	End GI2	23,220		18.31	19.09				20.30
Polar	Onset GI2	23,340		18.39	19.19	27.16			20.80
desert	EVT top			24.36	24.15	30.48			
	EVT base	24,720		24.44	24.16	30.57			
LEZ 5	End GI3	27,540	34.15	34.45	34.25				28.15
Forest-tundra	Onset GI3	27,780	34.75	35.04	34.95	36.73			28.55
	WBT top		36.66	36.80	36.83	37.80			28.80
	WBT base	28,100	36.90	37.02	36.89	37.92			28.92
	End GI4	28,600	39.55	39.82	39.63	39.88		9.19	29.10
	Onset GI4	28,900	39.95	40.17	40.10	40.18	3.30	9.49	29.90
	UT1 top		46.43	46.55	46.50	42.76	8.72		31.36
	UT1 base	30,300	46.59	46.68	46.59	42.91	8.80		31.41
LEZ 6	End GI5.2	32,040	54.25	54.31	54.44	43.92	10.35	18.30	33.35
Forest-steppe	Onset GI5.2	32,500	55.40	55.15	55.03	44.27	10.70	19.00	33.90
	End GI6	33,360	56.65	56.83	56.68	44.57	11.65	19.65	35.10
	Onset GI6	33,740	57.70	57.73	57.41		12.55	20.03	35.60
	End GI7	34,740	61.95	62.11	62.37			21.36	36.40
	Onset GI7c	35,480	63.15	63.32	63.84			22.22	36.85
LEZ 7	End GI8	36,580	65.35	65.43	65.47	46.26	14.50	23.87	37.90
Cold temperate	Onset GI8c	38,220	66.95	66.87	67.05	47.59	18.10	26.02	40.95
forest	End GI9	39,900	69.15	69.50	69.36	49.63	20.65		42.35
	Onset GI9	40,160	70.65	70.57	70.46	50.02	21.20		42.55
	DWT top		71.14	71.11	70.91		21.46		42.68
	DWT base	40,370	71.19	71.16	70.93		21.50		42.70
	End GI10	40,800	71.75	71.94	71.84		21.75		
	Onset GI10	41,460	73.15	72.77	72.60	51.01	22.50		
	End GI11	42,240	75,30	76.05	75.38		22.75	27.50	
	Onset GI11	43,340	77.15	76.42	76.46	53.54	23.55		43.60
	ACE top	43,500	77.20	76.60	76.62	53.60	24.08	28.00	43.61
	ACE base		77.94	77.10	76.94	56.97	24.33	29.00	44.00
	End GI12	44,280		77.49	77.07			30.02	
	Onset GI12c	46,860	78.35	78.20	77.87	56.99		30.80	46.40
	MMT top		81.60	81.74	81.16	57.58	28.07	31.94	47.43
	MMT base	47,340	81.63	81.78	81.17	57.63	28.14	31.95	47.45
	End GI13	48,340		88.02	87.77	58.28	29.80	35.60	47.80

Table 2. *Cont.*

LEZ	Time Marker	Age [yr b2k]	AU2 [m]	AU3 [m]	AU4 [m]	DE3 [m]	MS1 [m]	OW1 [m]	RM2 [m]
LEZ 8	Onset GI13c	49,280	88.30	89.92	89.61	59.72	32.55	36.18	48.45
Warm temperate	End GI14	49,600		90.87	90.50	60.07	33.20	36.33	49.10
forest	Onset GI14a	51,500		91.75	91.59	61.18			
	Onset GI14b	51,660		91.91	91.72	61.98			
	Onset GI14e	54,220	93.25	93.52	93.44	67.05	37.15	38.64	51.90
	End GI15.1	54,900		93.83	93.68				
	Onset GI15.1	55,000		93.85	93.70				
	End GI15.2	55,400	93.95	93.97	93.78	69.25		38.84	52.35
	Onset GI15.2	55,800	95.10	96.31	95.13	69.56		38.95	52.80
	End GI16	56,500	97.75	100.42	99.70	70.32		39.06	53.15
	Onset GI16.1c	58,040		101.28	101.17		38.80		
	End GI16.2	58,160		101.37	101.19				
	Onset GI16.2	58,280	100.95	101.45	101.31	73.81			53.80
	End GI17	58,560	101.70	101.65	101.64				
	Onset GI17.2	59,080	102.15	101.96	102.31				
	AUT top		102.33		102.38	76.24	39.80	39.42	56.39
	AUT base	59,130				76.30	39.86	39.58	56.58
	End GI18	63,840				78.35	46.35		62.40
	Onset GI18	64,100				78.43	46.65		62.80

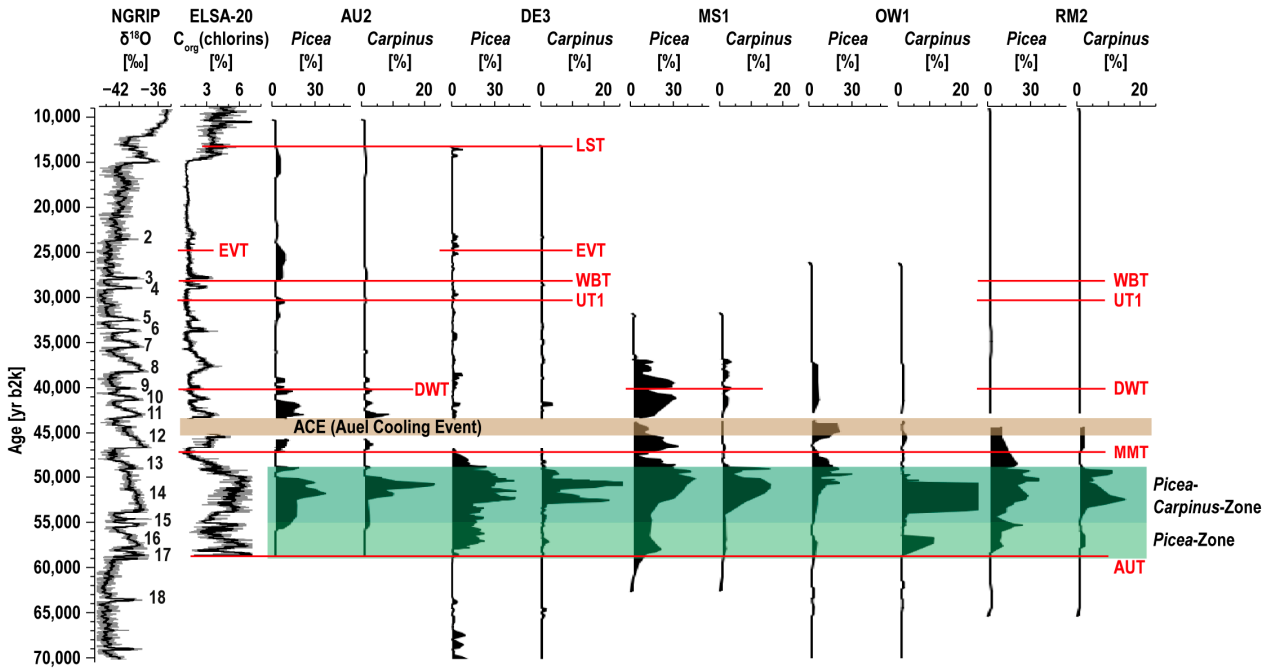

Figure 3. *Picea* and *Carpinus* pollen percentages versus age [6,7,13]. Highlighted in green are the *Picea*-Zone and the *Picea-Carpinus*-Zone, which represent the early MIS 3 warm phase forest covering the Eifel. Red lines represent marker tephra layers in each sediment core. Highlighted in brown is the Auel Cold Event (ACE), a massive slumping event in the maar records during GS12. Additionally shown are the interstadial succession (GI2–18) of NGRIP oxygen isotope time series [2] and the ELSA-20 C_{org}(chlorins) record [4]. Pollen counts were performed by Frank Dreher.

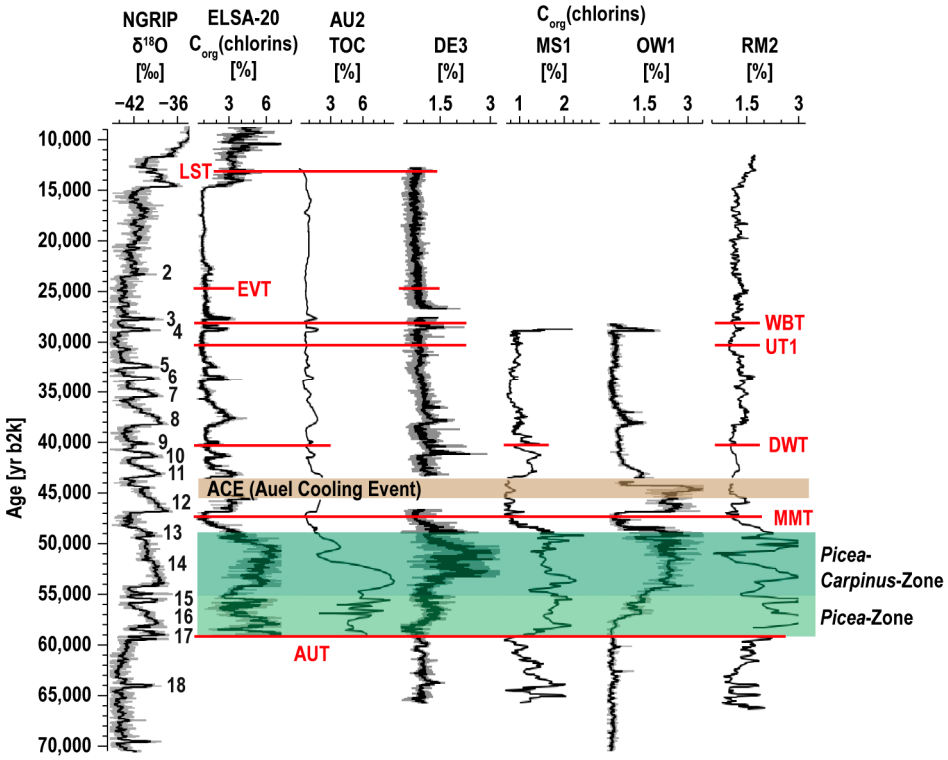

Figure 4. C_{org}(chlorins) records versus age. The *Picea*-Zone and the *Picea-Carpinus*-Zone are highlighted in green and red lines represent marker tephra layers in each sediment core. The Auel Cold Event (ACE) is highlighted in brown. Also shown are Greenland Interstadials 2–18 of NGRIP oxygen isotope time series [2], the ELSA-20 C_{org}(chlorins) data [4] and the total organic carbon (TOC) record of core AU2 [6]. For a detailed overview of stadial/interstadial succession and volcanic marker layers, see Table 2.

2.4. Pollen and Organic Carbon (Chlorins) Data

Pollen preparation was carried out according to the techniques of Berglund and Ralska-Jasiewiczowa [23] and Faegri and Iversen [24]. Sediment samples of 1 cm^3 volume were treated with potassium hydroxide solution (KOH), hydrochloric acid (HCl) and hydrofluoric acid (HF). Acetic acid ($C_2H_4O_2$) and a mixture (9:1) of acetic anhydride ($C_4H_6O_3$) and sulfuric acid (H_2SO_4) was used for acetolysis. Samples were centrifugated at 3000–3500 rpm for 5 min and then sieved at 200 µm and filtered at 10 µm. To calibrate absolute pollen concentration per cm^3, Lycopodium-spore tablets were added. Samples were mounted using liquid, anhydrous glycerol ($C_3H_8O_3$). Pollen counting was performed using a 600-fold magnification and a minimum of 300 pollen grains were counted for each sample. Because pollen analysis was intended to correlate the sediment cores to the early MIS 3 warm phase forest [6,7], only *Picea* and *Carpinus* percentages are presented in the pollen diagram (Figure 3).

Organic carbon (chlorins) content was determined with a Gretag Spectrolino. The measurement principle is based on the sediment reflectance of each wavelength relative to a white color standard over a 2.5-mm-wide area [25,26]. The absorption at the wavelength of 670 nm represents chlorophyll a, b and c and bacteriochlorophyll c and d as well as their derivates. This method can therefore be used to detect trends in the total aquatic palaeo-production in marine and lake sediments [26–28].

Cores AU3 and AU4, that make up the ELSA-20 record (Figure 4), as well as DE3 were measured in 1-mm-wide increments. OW1 was measured in 2-mm-wide and cores MS1 and RM2 in 5-cm-wide increments. Organic carbon (chlorins) contents of all presented cores were age-tuned to the ELSA-20 chronology [4] and the stadial/interstadial succession back to GI18 (Table 2, Figure 4) using identified marker tephra layers [9] as anchor points.

2.5. Flood and Slump Event Layers

Lacustrine basins are very well suited to study the frequency and intensity of past flood events due to their usually very slow and constant sedimentation rates. In contrast, rivers are often high-energy systems and information about prior events can easily be lost due to erosion effects [29,30]. Flood and slumping layers are typically characterized by their distinct sediment structures (Figure 5) and severe flood and slumping events can often be detected macroscopically directly on the sediment core (Figure 5B,D). Sediment cores were visually examined to identify slumps and flood layers thicker than 0.7 cm. This method, established by Brunck et al. [15], analyses the variance of flooding and slumping frequencies in the Eifel region during the stadial/interstadial succession and does not provide an absolute count of event layers.

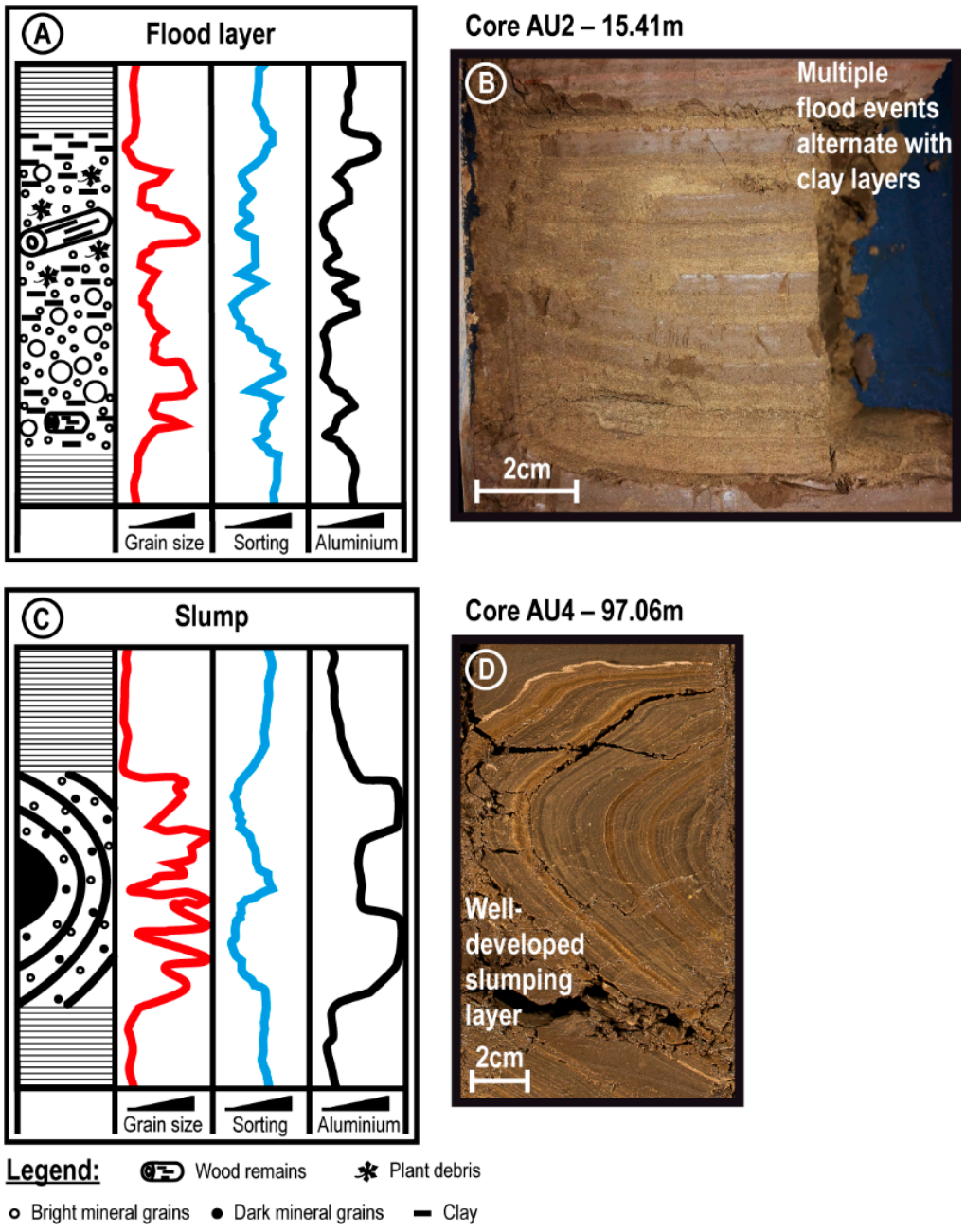

Figure 5. Typical characteristics of flood and slumping layers (after [15]). (**A**) Schematic illustration and (**B**) picture of an idealized flood layer. (**C**) Schematic illustration and (**D**) picture of an idealized slumping layer.

Regional discrepancies in frequency and temporal occurrence of slump and flood layers between the maars can be explained by differing geomorphologic settings and magnitudes of inflow, respectively. The Auel infilled maar basin, for example, has both the highest fluvial input and sedimentation rate (2 mm/a). This results in a greater sensitivity to floods in Auel and thus explains increased flood deposition and thicker flood layers. We therefore present a normalized flood index, i.e., the number of flood layers per millennium divided by the maximum number of flood layers per millennium for all cores (Figure 6).

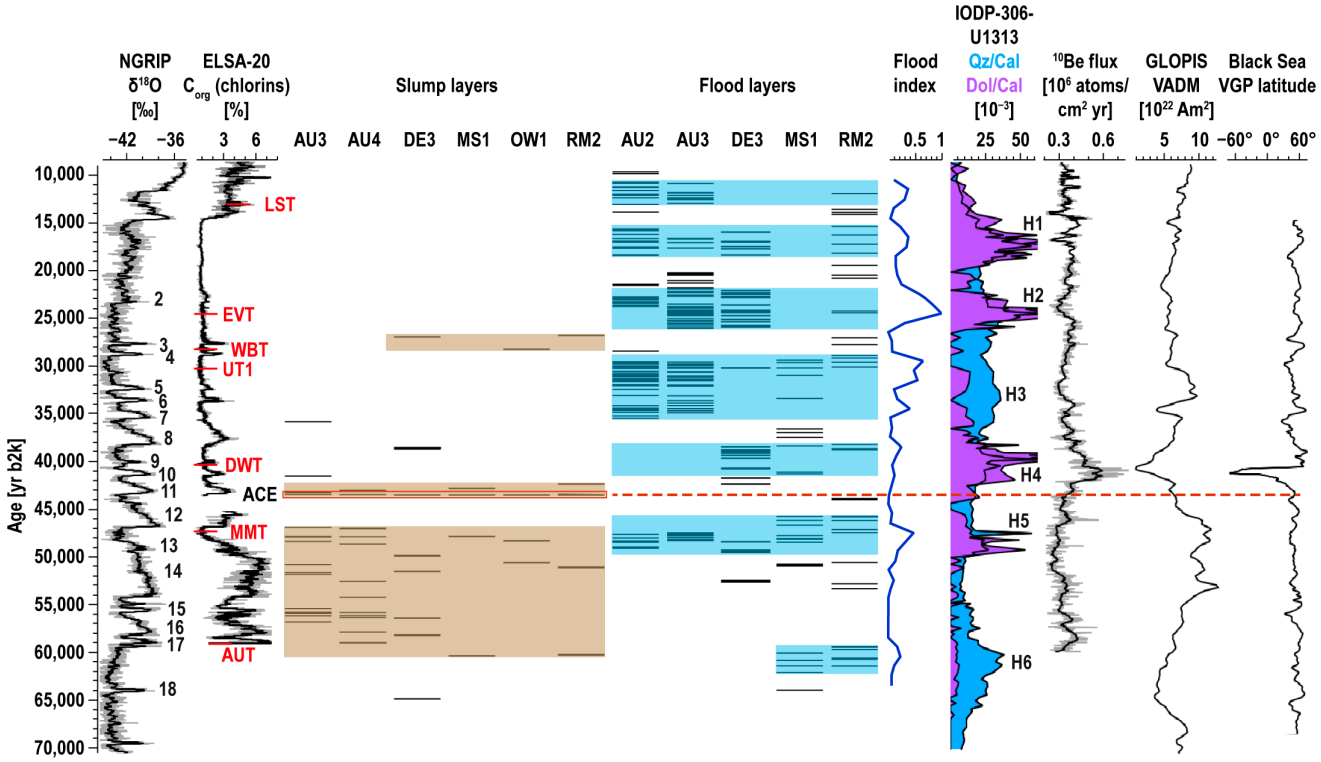

Figure 6. Phases of increased slumping with the ACE (Auel Cold Event) and flood activity in sediment cores (highlighted in brown and light blue, respectively) and normalized flood index (blue line). Additionally shown are Greenland Interstadials 2–18 of NGRIP oxygen isotope time series [2], the ELSA-20 C_{org}(chlorins) climate proxy record [4] with marker tephra layers (red abbreviations), identified Heinrich stadials (H1–6) in quartz/calcite (blue) and dolomite/calcite (purple) ratios from North Atlantic Site U1313 [31], the GLOPIS-75 relative paleo-intensity stack [32], virtual geomagnetic pole (VGP) latitudes from Black Sea sediments [33] and the composite ^{10}Be flux record from GRIP and GISP2 ice cores [34].

3. Results

3.1. Alignment of Cores

As illustrated in Figure 3, all cores show a long-lasting maximum of spruce (*Picea*) between GI17 and GI13. During GI14 and GI13, this *Picea*-Zone is further characterized by a prominent peak of hornbeam (*Picea-Carpinus*-Zone). These two phases represent the early MIS 3 warm phase forest covering the Eifel with abundant thermophilous tree pollen [6,7].

Although measured with different resolutions, the overall structures of the presented organic carbon (chlorins) records show clear similarities to the ELSA-20 [4] and NGRIP ice core [2] chronologies (Figure 4). This allows direct matching of the records using marker tephra layers [9] as anchor points. In particular, the early MIS 3 warm phase (GI17–13) is clearly visible in all cores as a distinct, long-lasting maximum in organic carbon (chlorins) production. Due to the maars' differing characteristics (e.g., geomorphologic setting, inflow rate), absolute organic carbon quantities vary between the cores (Figure 4). For example, the large catchment area of the Auel Maar results in an increased nutrient input into the

maar and therefore amplifies the organic carbon signal. Differences in the organic carbon (chlorins) production between interstadial periods are due to their differing lengths. Longer and more stable interstadial periods promoted a lush vegetation, which caused a higher nutrient input into the lakes. However, using the volcanic marker deposits as control points [9], almost all interstadial periods could be identified in the organic carbon (chlorins) records (Table 2).

3.2. Flood and Slump Frequencies

Periods of increased slumping as well as flooding frequency could be identified in all sediment records (Figure 6). Intervals of supra-local flood activity seem to align with Heinrich stadials in marine sediment records [31]. Flood frequency remained high throughout all Heinrich times. Phases of increased slumping activity occurred during the early MIS 3 warm phase (60,000–47,000 yr b2k), at 43,500 yr b2k and subsequent to GI3 (Figure 6). Slumps between 60,000 and 47,000 yr b2k and after GI3 are characterized by well-developed folding textures within the sediment ranging from several millimeters to tens of centimeters in thickness, quite contrary to the slumping event that occurred at 43,500 yr b2k.

The multi-proxy correlation reveals in all cores a massive slumping event during GS12 (Figure 7). Due to its unique characteristics in the Auel maar sediments (Figure 7A,B), we describe this as the Auel Cold Event (ACE). At its type locality, the ACE led to the formation of a slump with a fractured, breccia-like sediment texture. Fragments of fine-grained, unconsolidated sediment packages with distinctive edges between individual "blocks" suggest that the sediment was solidified due to deep frost conditions at around 43,500 yr b2k. Individual fragments are clearly distinguishable by color and can reach diameters of several centimeters, whereby larger blocks accumulate at the slump's base and smaller ones towards its top (Figure 7A,B). Extensive rotation of individual blocks suggest that the transported material has lost much of its original structure. In the Auel cores, the ACE thickness varies between 0.32 m (AU4), 0.50 m (AU3) and 0.74 m (AU2; Figures S2–S4).

In core DE3, the ACE has a total thickness of 3.37 m (Figure 7C). In the lower 3 m, it is characterized by well-developed, massive folds within the slumped sediment. Clearly visible fine laminations, even if in part extensively folded and tilted, indicate that the transported material has preserved most of its structural integrity. Overlying this folded segment is a breccia of unconsolidated, fine-grained sediments similar to the one described in the Auel cores (Figure 7D). However, in core DE3, fractured fragments only reach diameters of a few centimeters at the slump's base and several millimeters at its top.

Due to a lack of lamination, the ACE is hardly visible in cores MS1 and RM2 (Figures S6 and S7). Instead, the slumped segment is characterized by stained or spotted, clayey to silty sediments. However, a sediment texture similar to the Auel cores and DE3, even though faintly developed, is present in core RM2. ACE thickness is 0.25 m and 0.39 m in cores MS1 and RM2, respectively. In core OW1, a massive fold across an entire core meter (28–29 m; Figure S8) representing the ACE shows that the transported sediment has maintained its structural integrity on a large scale.

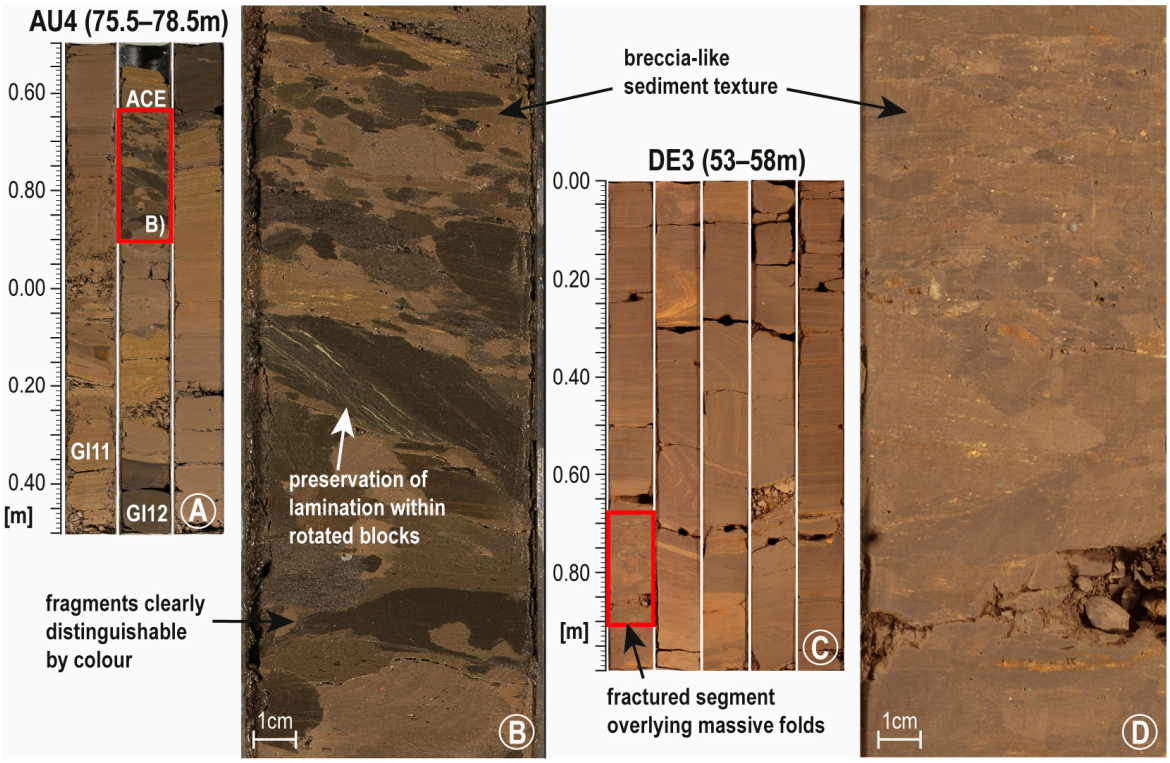

Figure 7. The Auel Cold Event (ACE). (**A**) ACE sediment slump in core AU4. (**B**) Enlarged segment showing a distinct breccia-like sediment texture within the slump with individual fragments clearly distinguishable. (**C**) ACE sediment slump in core DE3 and (**D**) enlarged segment of its breccia-like texture.

4. Discussion

4.1. Flood Phases during the Last 65,000 Years

Variations in flood dynamics are climatically driven, either directly by an increased water supply or indirectly via vegetation changes and/or permafrost. Shifts in flood frequency represent climate responses within the catchment area and elevated flood activity mainly reflects climate transitions into colder periods when a decline in vegetation cover decreases soil stability and therefore elevates the erosion potential [15,35].

Phases of increased and supra-local flood activity in the Eifel region match Heinrich stadials in marine sediment records (Figure 6) [31], which are associated with increased aeolian dust flux during spring [14] and extensive glacial advances into the North Atlantic (e.g., [36,37]). Repeated flood deposition throughout all Heinrich times suggest a vegetation response within the catchment area to emerging and persisting cold climate conditions. The increased water runoff into the maar during Heinrich stadials is likely to have originated from heavy rain events or seasonal snowmelt, which could easily erode the destabilized sediments.

4.2. Frost at 43,500 b2k

A prominent slumping layer during GS12 (ACE), which is not associated with Heinrich stadial times, stands out in the presented maar records. Slumped segments with distinctive fine-grained sediment fragments and a breccia-like texture, that shows a preservation of lamination within rotated blocks, in the Auel sediment records and other maars (Figure 7) indicate that the lakes' flanks must have been frozen when this slumping event occurred. This suggests that the region was exposed to deep frost at around 43,500 yr b2k. Rapid thawing and/or seismic activity must have then caused solifluction of the lake sediments. Other authors indeed portray this stadial as a severe cooling step across Europe with deep frost or permafrost conditions (e.g., [38,39]). A loess-paleosol sequence at the archaeological site Willendorf II (Austria) features a well-developed frost layer, confined by two paleosols representing GI11 and 12, respectively [40]. Further evidence can be

found in a loess-paleosol record in Northern France, where a distinct permafrost horizon was dated to 43–44 ka calBP [39]. Vandenberghe and van der Pflicht [41] propose that the Hasselo stadial, which is represented by ice-wedge cast horizons in silty sediment deposits at its type localities in Eastern [42] and Northern Netherlands [43] and was dated to 43,220–42,290 calBP, is likely to correspond to GS12. In the East and South Carpathians, a hiatus and a very prominent $\delta^{13}C$ maximum (dated to 43.3–44 kaU-Th) in two speleothem stable isotope records, respectively, indicate that a rapid shift towards cold and arid stadial conditions occurred within a few decades in Eastern Europe, at least in higher altitudes [38].

The fact that such a distinctive slumping event with such a unique sediment texture occurred simultaneously in several maar lakes many kilometers apart, during a period when deep frost conditions prevailed in the region, suggests that this event was not caused by local factors such as geomorphology of the lakes. Instead, either a rapid, unstable climate shift that differs significantly from other GS/GI transitions or some other major geological phenomenon must have triggered this massive slumping activity. One important event that took place around that time is the onset of the Laschamp geomagnetic excursion, during which the Earth's magnetic field strength was significantly reduced and reversed (Figure 6) (e.g., [32,33]). This caused a considerable enhanced flux of high-energy protons from the sun into the atmosphere [34], affecting ozone levels globally [44]. UV-B radiation levels in Europe increased by 10–20% due to significant ozone depletion down to latitudes of 40–45° [45,46]. Although the reversed polarity phase occurred between 40–41 ka (e.g., [47,48]), an initial weakening of the magnetic field strength can be observed as a short-termed, yet distinctive, increase in the ^{10}Be flux record during GS12 [34]. This could have caused increasingly unstable climate conditions in the region which triggered massive slumping activity at the maars' thawing slopes.

Albeit that direct impacts of geomagnetic excursions and reversals and their underlying mechanisms are still debated in the literature, a connection to geological and ecological phenomena such as increased seismic activity and volcanism, major global climate shifts, long-term sea level changes and species extinctions have been proposed (e.g., [49–55]). Cooper et al. [44] suggest that the weakening of the geomagnetic field directly preceding the reversed state of the Laschamp event promoted major climate changes, extinction events and shifts in the archaeological record on a global scale.

The climate and environmental deteriorations after GI13 are thought to be at least partly responsible for European Neanderthal depopulation and the subsequent territorial expansion of anatomically modern humans [38,40,56–58]. This cultural transition, which is known as the Middle-Upper Paleolithic transition, is documented across Europe as a severe drop in population density [59], as well as shifts in hunted species [60] and distinct artefact assemblages at archaeological sites [56,61,62]. The harsh climate conditions during the GS12 permafrost period and Heinrich stadial 4 likely forced European populations to track their preferred habitats or change their subsistence strategies in order to survive [63]. The environmental impacts caused by the Laschamp excursion and the Campanian Ignimbrite eruption, a massive volcanic eruption in South Italy approximately 40,000 years ago [64,65], could have then taken further toll on stricken regional populations (Figure 8) [66–69]. Several archaeological sites in the upper and middle Danube Valley propose a widespread Neanderthal depopulation across Europe during this time period and a subsequent repopulation by anatomically modern humans (e.g., [70,71]). During these major ecological challenges, modern humans probably had the advantage of innovative technologies and improved sociality over the Neanderthals, which might have helped them to better adapt to their changing environment [38,56]. The latest directly dated Neanderthal remains of central Europe range from 40.66–41.95 ka calBP [72,73], which coincides exactly with the age of the Laschamp geomagnetic reversal.

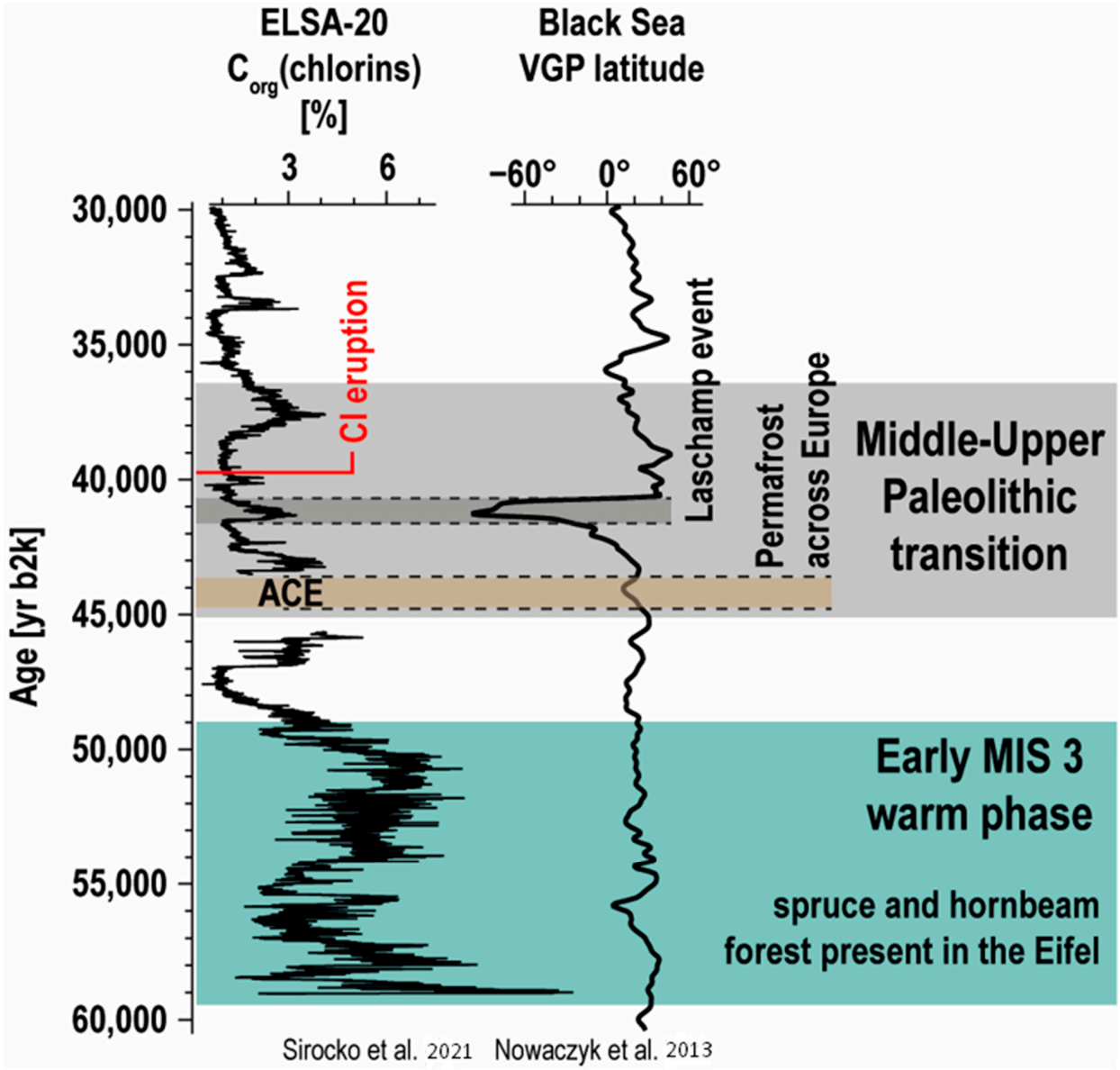

Figure 8. The Middle-Upper Paleolithic transition. Severely cold and arid climate conditions during Greenland Stadial 12 (e.g., [38,40]), as well as the environmental impacts of the Campanian Ignimbrite volcanic eruption [4,66,67] and Laschamp geomagnetic event [33,68,69] occurred during the transition from Neanderthals to modern humans as the dominant species in Europe.

5. Conclusions

During the past 65,000 years, the climate of the Eifel gradually transitioned from the early MIS 3 warm phase forest into the icy desert of the LGM [6,7]. Throughout this time, phases of increased flood deposition and slumping activity affected the maar lakes of the region:

- Phases of increased and supra-local flood activity coincide with Heinrich stadials in marine sediment records,
- Flood frequency remained high throughout all Heinrich stadials,
- Flood deposition was caused by a decline in stabilizing vegetation cover due to detrimental climate conditions and increased water supply from heavy rains or seasonal snowmelt,
- Periods of high slumping activity occurred during the early MIS 3 warm phase, at 43,500 yr b2k and subsequent to GI3,

- The slumping event at 43,500 b2k (ACE) led to the formation of a prominent fractured, breccia-like sediment texture with a preservation of lamination within individual rotated blocks, indicating that the sediment was solidified due to deep frost conditions during GS12,
- The timing of the ACE coincides with the initial onset of the Laschamp geomagnetic excursion [32–34].

Although a definite connection between the ACE and the Laschamp event cannot be proven, their simultaneous timing seems intriguing. Nonetheless, the severely cold climate conditions during GS12, as well as the environmental impacts of the Laschamp and the Campanian Ignimbrite events, must have presented major challenges for European populations [66–69] and are quite likely responsible for the demise of the Neanderthals and the subsequent domination of anatomically modern humans.

Supplementary Materials: The following supporting information can be downloaded at: https://www.mdpi.com/article/10.3390/quat6010014/s1, Figure S1: Age/depth models of cores AU2, DE3, MS1, OW1 and RM2 on basis of ELSA-20 stratigraphy [4]. Red circles represent exposed marker tephra layers in each core (LST—Laacher See Tephra [17]; EVT—Eltville Tephra; WBT—Wartgesberg Tephra; UT1—Unknown Tephra 1; DWT—Dreiser Weiher Tephra; MMT—Meerfelder Maar Tephra; AUT—Auel Maar Tephra); Figure S2: Core photo of sediment record AU2 with Auel Cold Event (ACE) and ages of marker tephra layers [4,17]. Ages of marker layers are given in the yr b2k notation; Figure S3: Core photo of sediment core AU3 with the Auel Cold Event (ACE) and ages of marker tephra layers [4,17]. Ages of marker layers are given in the yr b2k notation; Figure S4: Core photo of sediment core AU4 with the Auel Cold Event (ACE) and ages of marker tephra layers [4,17]. Ages of marker layers are given in the yr b2k notation; Figure S5: Core photo of sediment core DE3 with the Auel Cold Event (ACE) and ages of marker tephra layers [4,17]. Ages of marker layers are given in the yr b2k notation; Figure S6: Core photo of sediment core MS1 with the Auel Cold Event (ACE) and ages of marker tephra layers [4,17]. Ages of marker layers are given in the yr b2k notation; Figure S7: Core photo of sediment core RM2 with the Auel Cold Event (ACE) and ages of marker tephra layers [4,17]. Ages of marker layers are given in the yr b2k notation; Figure S8: Core photo of sediment core OW1 with the Auel Cold Event (ACE) and ages of marker tephra layers [4,17]. Ages of marker layers are given in the yr b2k notation.

Author Contributions: Conceptualization, J.A. and F.S.; methodology, J.A.; validation, F.S.; investigation, J.A.; resources, F.S.; writing—original draft preparation, J.A.; writing—review and editing, F.S.; visualization, J.A.; supervision, F.S. All authors have read and agreed to the published version of the manuscript.

Funding: This research was funded by the Johannes Gutenberg-University of Mainz.

Data Availability Statement: All data will be downloadable at our university website (https://www.klimaundsedimente.geowissenschaften.uni-mainz.de).

Acknowledgments: Drilling of the cores was done by the drilling company "Stölben Bohr" (Cochem, Germany). Pollen preparation and counts were performed by Frank Dreher and Sarah Britzius. Michael Förster, Anastasia Zemlitskaya and Fiona Schenk sampled and counted marker tephra layers. We thank the student assistants at Mainz University for measuring organic carbon (chlorins) contents of the sediment cores, Petra Sigl for her help with the illustrations and Sarah Britzius for her contribution to the discussion. Furthermore, we would like to thank the anonymous reviewers for their thoughtful and valuable comments on the manuscript.

Conflicts of Interest: The authors declare no conflict of interest.

References

1. North Greenland Ice Core Project Members. High-resolution record of Northern Hemisphere climate extending into the last interglacial period. *Nature* **2004**, *431*, 147–151. [CrossRef]
2. Rasmussen, S.O.; Bigler, M.; Blockley, S.P.; Blunier, T.; Buchardt, S.L.; Clausen, H.B.; Cvijanovic, I.; Dahl-Jensen, D.; Johnsen, S.J.; Fischer, H.; et al. A stratigraphic framework for abrupt climatic changes during the Last Glacial period based on three synchronized Greeland ice-core records: Refining and extending the INTIMATE event stratigraphy. *Quat. Sci. Rev.* **2014**, *106*, 14–28. [CrossRef]

3. Svensson, A.; Andersen, K.K.; Bigler, M.; Clausen, H.B.; Dahl-Jensen, D.; Davies, S.M.; Johnsen, S.J.; Muscheler, R.; Parrenin, F.; Rasmussen, S.O.; et al. A 60 000 year Greenland stratigraphic ice core chronology. *Clim. Past.* **2008**, *4*, 47–57. [CrossRef]
4. Sirocko, F.; Martinez-García, A.; Mudelsee, M.; Albert, J.; Britzius, S.; Christl, M.; Diehl, D.; Diensberg, B.; Friedrich, R.; Fuhrmann, F.; et al. Multidecadal climate variability in central Europe over the past 60,000 years. *Nat. Geosci.* **2021**, *14*, 651–658. [CrossRef]
5. Fletcher, W.J.; Sánchez Goñi, M.F.; Allen, J.R.M.; Cheddadi, R.; Combourieu-Nebout, N.; Huntley, B.; Lawson, I.; Londeix, L.; Magri, D.; Margari, V.; et al. Millennial-scale variability during last glacial in vegetation records from Europe. *Quat. Sci. Rev.* **2010**, *29*, 2839–2864. [CrossRef]
6. Sirocko, F.; Knapp, H.; Dreher, F.; Förster, M.W.; Albert, J.; Brunck, H.; Veres, D.; Dietrich, S.; Zech, M.; Hambach, U.; et al. The ELSA-Vegetation-Stack: Reconstruction of Landscape Evolution Zones (LEZ) from laminated Eifel maar sediments of the last 60,000 years. *Glob. Planet Chang.* **2016**, *142*, 108–135. [CrossRef]
7. Sirocko, F.; Albert, J.; Britzius, S.; Dreher, F.; Martínez-García, A.; Dosseto, A.; Burger, J.; Terberger, T.; Haug, G. Threshold for the presence of glacial megafauna in central Europe during the last 60,000 years. *Nat. Sci. Rep.* **2022**, *12*, 20055. [CrossRef] [PubMed]
8. Büchel, G. *Vulkanologische Karte der West-und Hocheifel*; Landesvermessungsamt Rheinland-Pfalz: Koblenz, Germany, 1994.
9. Förster, M.W.; Sirocko, F. Volcanic activity in the Eifel during the last 500,000 years: The ELSA-Tephra-Stack. *Glob. Planet Chang.* **2016**, *142*, 100–107. [CrossRef]
10. Förster, M.W.; Zemlitskaya, A.; Otter, L.; Buhre, S.; Sirocko, F. Late Pleistocene Eifel eruptions: Insights from clinopyroxene and glass geochemistry of tephra layers from Eifel Laminated Sediment Archive sediment cores. *J. Quat. Sci.* **2019**, *35*, 186–198. [CrossRef]
11. Seelos, K.; Sirocko, F.; Dietrich, S. A continuous high-resolution dust record for the reconstruction of wind systems in central Europe (Eifel, Western Germany) over the past 133 ka. *Geophys. Res. Lett.* **2009**, *36*, L20712. [CrossRef]
12. Sirocko, F.; Seelos, K.; Schaber, K.; Rein, B.; Dreher, F.; Diehl, M.; Lehne, R.; Jäger, K.; Krbetschek, M.; Degering, D. A late Eemian aridity pulse in central Europe during the last glacial interception. *Nature* **2005**, *436*, 833–836. [CrossRef] [PubMed]
13. Sirocko, F.; Dietrich, S.; Veres, D.; Grootes, P.; Schaber-Mohr, K.; Seelos, K.; Nadeau, M.-J.; Kromer, B.; Rothacker, L.; Röhner, M.; et al. Multi-Proxy-Dating of Holocene maar lakes and Pleistocene dry maar sediments in the Eifel, Germany. *Quat. Sci. Rev.* **2013**, *62*, 56–72. [CrossRef]
14. Fuhrmann, F.; Diensberg, B.; Gong, X.; Lohmann, G.; Sirocko, F. Aridity synthesis for eight selected key regions of the global climate system during the last 60 000 years. *Clim. Past* **2020**, *16*, 2221–2238. [CrossRef]
15. Brunck, H.; Sirocko, F.; Albert, J. The ELSA-Flood-Stack: A reconstruction from the laminated sediments of Eifel maar structures during the last 60 000 years. *Glob. Planet Chang.* **2016**, *142*, 136–146. [CrossRef]
16. Brauer, A.; Endres, C.; Negendank, J.F.W. Lateglacial calendar year chronology based on annually laminated sediments from Lake Meerfelder Maar, Germany. *Quat. Int.* **1999**, *61*, 17–25. [CrossRef]
17. Reinig, F.; Wacker, L.; Jöris, O.; Oppenheimer, C.; Guidobaldi, G.; Nievergelt, D.; Adolphi, F.; Cherubini, P.; Engels, S.; Esper, J.; et al. Precise date for the Laacher See eruption synchronizes the Younger Dryas. *Nature* **2021**, *595*, 66–69. [CrossRef]
18. Ampel, L.; Wohlfarth, B.; Risberg, J.; Veres, D. Paleolimnological response to millennial and centennial scale climate variability during MIS 3 and 2 as suggested by the diatom record in Les Echets. *Quat. Sci. Rev.* **2008**, *27*, 1493–1504. [CrossRef]
19. Wohlfarth, B.; Veres, D.; Ampel, L.; Lacourse, T.; Blaauw, M.; Preusser, F.; Andrieu-Ponel, V.; Keravis, D.; Lallier-Vergès, E.; Björck, S.; et al. Rapid ecosystem response to abrupt climate changes during the last glacial period in Western Europe, 40–16 ka. *Geology* **2008**, *36*, 407–410. [CrossRef]
20. Wernli, H.; Pfahl, S. Grundlage des Klimas und extremer Wettersituationen. In *Wetter, Klima, Menschheitsentwicklung. Von der Eiszeit bis ins 21. Jahrhundert*; Sirocko, F., Ed.; Theiss: Stuttgart, Germany, 2009; pp. 44–52.
21. Seib, N.; Kley, J.; Büchel, G. Identification of maars and similar volcanic landforms in the West Eifel Volcanic Field through image processing of DTM data: Efficiency of different methods depending on preservation state. *Int. J. Earth Sci.* **2013**, *102*, 875–901. [CrossRef]
22. Engels, S.; Bohncke, S.J.P.; Heiri, O.; Schaber, K.; Sirocko, F. The lacustrine sediment record of Oberwinkler Maar (Eifel, Germany): Chironomid and macro-remain-based inferences of environmental changes during Oxygen Isotope Stage 3. *Boreas* **2008**, *37*, 414–425. [CrossRef]
23. Berglund, B.E.; Ralska-Jasiewiczowa, M. Pollen analysis and pollen diagrams. In *Handbook of Holocene Palaoecology and Palaeohydrology*; Berglund, B.E., Ed.; John Wiley and Sons: New York, NY, USA, 1986; pp. 455–484.
24. Faegri, K.; Iversen, J. *Textbook of Pollen Analysis*; John Wiley and Sons: Chichester, UK, 1989.
25. Rein, B.; Sirocko, F. In-situ reflectance spectroscopy—Analysing techniques for high resolution pigment 300 logging sin sediment cores. *Int. J. Earth Sci.* **2002**, *91*, 950–954. [CrossRef]
26. Butz, C.; Grosjean, M.; Fischer, D.; Wunderle, S.; Tylmann, W.; Rein, B. Hyperspectral imaging spectroscopy: A promising method for the biogeochemical analysis of lake sediments. *J. Appl. Remote Sens.* **2015**, *9*, 096031. [CrossRef]
27. Michelutti, N.; Smol, J.P. Visible spectroscopy reliably tracks trends in paleo-production. *J. Paleolimnol.* **2016**, *56*, 253–265. [CrossRef]
28. Sanchini, A.; Grosjean, M. Quantification of chlorophyll a, chlorophyll b and pheopigments a in lake sediments through deconvolution of bulk UV-VIS absorption spectra. *J. Paleolimnol.* **2020**, *64*, 243–256. [CrossRef]
29. Macklin, M.G. Holocene River Environments in Prehistoric Britain: Human Interaction and Impact. *J. Quat. Sci.* **1999**, *14*, 521–530. [CrossRef]

30. Thorndycraft, V.R.; Benito, G.; Rico, M.; Sopea, A.; Sánchez-Moya, Y.; Casas, A. A long-term flood discharge record derived from slackwater flood deposits of the Llobregat River, NE Spain. *J. Hydrol.* **2005**, *313*, 16–31. [CrossRef]
31. Naafs, B.D.A.; Hefter, J.; Grützner, J.; Stein, R. Warming of surface waters in the mid-latitude North Atlantic during Heinrich events. *Paleoceanogr* **2013**, *28*, 153–163. [CrossRef]
32. Laj, C.; Kissel, C.; Beer, J. High Resolution Global Paleointensity Stack Since 75 kyr (GLOPIS-75) Calibrated to Absolute Values. In *Timescales of the Paleomagnetic Field*; Channell, J.E.T., Kent, D.V., Lowrie, W., Meert, J.G., Eds.; Am Geophys Union: Washington, DC, USA, 2004; pp. 255–265.
33. Nowaczyk, N.R.; Frank, U.; Kind, J.; Arz, H.W. A high-resolution paleointensity stack of the past 14 to 68 ka from Black Sea sediments. *Earth Planet Sci. Lett.* **2013**, *384*, 1–16. [CrossRef]
34. Muscheler, R.; Beer, J.; Wagner, G.; Laj, C.; Kissel, C.; Raisbeck, G.M.; Yiou, F.; Kubik, P.W. Changes in the carbon cycle during the last deglaciation as indicated by the comparison of ^{10}Be and ^{14}C records. *Earth Planet Sci. Lett.* **2004**, *219*, 325–340. [CrossRef]
35. Vandenberghe, J. Climate forcing of fluvial system development: An evolution of ideas. *Quat. Sci. Rev.* **2003**, *22*, 2053–2060. [CrossRef]
36. Broeker, W.; Bond, G.; Klas, M.; Clark, E.; McManus, J. Origin of the northern Atlantic's Heinrich events. *Clim. Dyn.* **1992**, *6*, 265–273. [CrossRef]
37. Hemming, S.R. Heinrich events: Massive late Pleistocene detritus layers of the North Atlantic and their global climate imprint. *Rev. Geophys.* **2004**, *42*, RG1005. [CrossRef]
38. Staubwasser, M.; Drăgușin, V.; Onac, B.P.; Assonov, S.; Ersek, V.; Hoffmann, D.L.; Veres, D. Impact of climate change on the transition of Neanderthals to modern humans in Europe. *Proc. Natl. Acad. Sci. USA* **2018**, *115*, 9116–9121. [CrossRef] [PubMed]
39. Antoine, P.; Coutard, S.; Guerin, G.; Deschodt, L.; Goval, E.; Locht, J.-L.; Paris, C. Upper Pleistocene loess-paleosol records from Northern France in the European context: Environmental background and dating of the Middle Palaeolithic. *Quat. Int.* **2016**, *411*, 4–24. [CrossRef]
40. Nigst, P.R.; Haesaerts, P.; Damblon, F.; Frank-Fellner, C.; Mallol, C.; Viola, B.; Götzinger, M.; Niven, L.; Trnka, G.; Hublin, J.-J. Early modern human settlement of Europe north of the Alps occurred 43,500 years ago in a cold steppe-type environment. *Proc. Natl. Acad. Sci. USA* **2014**, *111*, 14394–14399. [CrossRef]
41. Vandenberghe, J.; van der Pflicht, J. The age of the Hengelo interstadial revisited. *Quat Geochro* **2016**, *32*, 21–28. [CrossRef]
42. Van Huissteden, J. Tundra rivers of the last glacial: Sedimentation and geomorphological processes during the Middle Pleniglacial (Eastern Netherlands). *Meded. Rijks Geol. Dienst.* **1990**, *44*, 1–138.
43. Kasse, C.; Vandenberghe, J.; Bohncke, S.J.P. Climate change and fluvial dynamics of the Maas during the Late Weichselian and Early Holocene. In *European River Activity and Climate Change During the Lateglacial and Early Holocene*; Frenzel, B., Vandenberghe, J., Kasse, C., Bohncke, S., Gläser, B., Eds.; VU Research Portal: Amsterdam, The Netherlands, 1995; Volume 14, pp. 123–150.
44. Cooper, A.; Turney, C.S.M.; Palmer, J.; Hogg, A.; McGlone, M.; Wilmhurst, J.; Lorrey, A.M.; Heaton, T.J.; Russell, J.M.; McCracken, K.; et al. A global environmental crisis 42,000 years ago. *Science* **2021**, *371*, 811–818. [CrossRef] [PubMed]
45. Vogt, J.; Zieger, B.; Glassmeier, K.-H.; Stadelmann, A.; Kallenrode, M.-B.; Sinnhuber, M.; Winkler, H. Energetic particles in the paleomagnetosphere: Reduced dipole configurations and quadrupolar contributions. *J. Geophys. Res.* **2007**, *112*, A06216. [CrossRef]
46. Winkler, H.; Sinnhuber, M.; Notholt, J.; Kallenrode, M.-B.; Steinhilber, F.; Vogt, J.; Zieger, B.; Glassmeier, K.-H.; Stadelmann, A. Modeling impacts of geomagnetic field variations on middle atmospheric ozone responses to solar proton events on long timescales. *J. Geophys. Res.* **2008**, *113*, D02302. [CrossRef]
47. Singer, B.S.; Guillou, H.; Jicha, B.R.; Laj, C.; Kissel, C.; Beard, B.L.; Johnson, C.M. ^{40}Ar/^{39}Ar, K-Ar and ^{230}Th–^{238}U dating of the Laschamp excursion: A radioisotopic tie-point for ice core and climate chronologies. *Earth Planet Sci. Lett.* **2009**, *286*, 80–88. [CrossRef]
48. Channell, J.E.T.; Hodell, D.A.; Curtis, J.A. ODP Site 1063 (Bermuda Rise) revisited: Oxygen isotopes, excursions, and paleointensity in the Brunhes chron. *Geochem. Geophys. Geosyst.* **2012**, *13*, Q02001. [CrossRef]
49. Raup, D.M. Magnetic reversals and mass extinctions. *Nature* **1985**, *314*, 341–343. [CrossRef]
50. Böhnel, H.; Reismann, N.; Jäger, G.; Haverkamp, U.; Negendank, J.F.W.; Schmincke, H.-U. Paleomagnetic investigation of the Quaternary West Eifel volcanics (Germany): Indication for increased volcanic activity during geomagnetic excursion/event? *J. Geophys.* **1987**, *62*, 50–61.
51. Marzocchi, W.; Mulargia, F.; Paruolo, P. The correlation of geomagnetic reversals and mean sea level in the last 150 m.y. *Earth Planet Sci. Lett.* **1992**, *111*, 383–393. [CrossRef]
52. Meert, J.G.; Levashova, N.M.; Bazhenov, M.L.; Landing, E. Rapid changes of magnetic Field polarity in the late Ediacaran: Linking the Cambrian evolutionary radiation and increased UV-B radiation. *Gondwana. Res.* **2016**, *34*, 149–157. [CrossRef]
53. Pavlov, V.E.; Fluteau, F.; Latyshev, A.V.; Fetisova, A.M.; Elkins-Tanton, L.T.; Black, B.A.; Burgess, S.D.; Veselovskiy, R.V. Geomagnetic secular variations at the Permian-Triassic boundary and pulsed magmatism during the eruption of the Siberian Traps. *Geochem. Geophys. Geosyst.* **2019**, *20*, 773–791. [CrossRef]
54. Herndon, J.M. Causes and consequences of geomagnetic field collapse. *J. Geog. Environ. Earth Sci. Int.* **2020**, *24*, 60–76. [CrossRef]
55. Herndon, J.M. Scientific basis and geophysical consequences of geomagnetic reversals and excursions: A fundamental statement. *J. Geog. Environ. Earth Sci. Int.* **2021**, *25*, 59–69. [CrossRef]

56. Conard, N.J.; Bolus, M.; Goldberg, P.; Münzel, S. The last Neanderthals and first modern humans in the Swabian Jura. In *When Neanderthals and Modern Human Met*; Conard, N.J., Ed.; Kerns Verlag: Tübingen, Germany, 2006; pp. 305–342.
57. Conard, N.J.; Bolus, M. Radiocarbon dating in the late Middle Paleolithic and the Aurignacian of the Swabian Jura. *J. Hum. Evolut.* **2008**, *55*, 886–897. [CrossRef]
58. Obreht, I.; Hambach, U.; Veres, D.; Zeeden, C.; Bösken, J.; Stevens, T.; Marković, S.B.; Klasen, N.; Brill, D.; Burow, C.; et al. Shift of large-scale atmospheric systems over Europe during late MIS 3 and implications for Modern Human dispersal. *Sci. Rep.* **2017**, *7*, 5848. [CrossRef] [PubMed]
59. Morin, E. Evidence for declines in human population densities during the early Upper Paleolithic in western Europe. *Proc. Natl. Acad. Sci. USA* **2008**, *105*, 48–53. [CrossRef] [PubMed]
60. Discamps, E.; Jaubert, J.; Bachellerie, F. Human choices and environmental constraints: Deciphering the variability of large game procurement from Mousterian to Aurignacian times (MIS 5–3) in southwestern France. *Quat. Sci. Rev.* **2011**, *30*, 2755–2775. [CrossRef]
61. Hoffecker, J.F. The spread of modern humans in Europe. *Proc. Natl. Acad. Sci. USA* **2009**, *106*, 16040–16045. [CrossRef]
62. Hublin, J.-J. The modern human colonization of western Eurasia: When and where? *Quat. Sci. Rev.* **2015**, *118*, 194–210. [CrossRef]
63. Rendu, W.; Renou, S.; Soulier, M.-C.; Rigaud, S.; Roussel, M.; Soressi, M. Subsistence strategy changes during Middle to Upper Paleolithic transition of Human Populations to their environment. *Sci. Rep.* **2019**, *9*, 15817. [CrossRef]
64. Giaccio, B.; Hajdas, I.; Isaia, R.; Deino, A.; Nomade, S. High-precision ^{14}C and ^{40}Ar/^{39}Ar dating of the Campanian Ignimbrite (Y-5) reconciles the time-scales of climatic-cultural processes at 40 ka. *Sci. Rep.* **2017**, *7*, 45940. [CrossRef]
65. Wulf, S.; Hardiman, M.J.; Staff, R.A.; Koutsodendris, A.; Appelt, O.; Blockley, S.P.E.; Lowe, J.J.; Manning, C.J.; Ottolini, L.; Schmitt, A.K.; et al. The marine isotope stage 1–5 cryptotephra record of Tenaghi Philippon, Greece: Towards a detailed tephrostratigraphic framework for the Eastern Mediterranean region. *Quat. Sci. Rev.* **2018**, *186*, 236–262. [CrossRef]
66. Fedele, F.G.; Giaccio, B.; Hajdas, I. Timescales and cultural process at 40,000 BP in the light of the Campanian Ignimbrite eruption, Western Eurasia. *J. Hum. Evolut.* **2008**, *55*, 834–857. [CrossRef]
67. Fitzsimmons, K.E.; Hambach, U.; Veres, D.; Iovita, R. The Campanian Ignimbrite Eruption: New Data on Volcanic Ash Dispersal and Its Potential Impact on Human Evolution. *PLoS ONE* **2013**, *8*, e65839. [CrossRef]
68. Norval, M.; Cullen, A.P.; de Gruijl, F.R.; Longstreth, J.; Takizawa, Y.; Lucas, R.M.; Noonan, F.P.; Van der Leun, J.C. The effects on human health from stratospheric ozone depletion and its interactions with climate change. *Photochem. Photobiol. Sci.* **2007**, *6*, 232–251. [CrossRef]
69. Valet, J.-P.; Valladas, H. The Laschamp-Mono lake geomagnetic events and the extinction of Neanderthal: A causal link or a coincidence? *Quat. Sci. Lett.* **2010**, *29*, 3887–3893. [CrossRef]
70. Conard, N.J.; Bolus, M. Radiocarbon dating the appearance of modern humans and timing of cultural innovations in Europe: New results and new challenges. *J. Hum. Evolut.* **2003**, *44*, 331–371. [CrossRef] [PubMed]
71. Higham, T.; Basell, L.; Jacobi, R.; Wood, R.; Bronk Ramsey, C.; Conard, N.J. Testing models for the beginning of the Aurignacian and the advent of figurative art and music: The radiocarbon chronology of Geißenklösterle. *J. Hum. Evolut.* **2012**, *62*, 664–676. [CrossRef]
72. Hublin, J.-J.; Talamo, S.; Julien, M.; David, F.; Connet, N.; Bodu, P.; Vandermeersch, B.; Richards, M.P. Radiocarbon dates from the Grotte du Renne and Saint-Césaire support a Neandertal origin for the Châtelperronian. *Proc. Natl. Acad. Sci. USA* **2012**, *109*, 18743–18748. [CrossRef] [PubMed]
73. Semal, P.; Rougier, H.; Crevecoeur, I.; Jungels, C.; Flas, D.; Hauzeur, A.; Maureille, B.; Germonpré, M.; Bocherens, H.; Pirson, S.; et al. New data on the late Neanderthals: Direct dating of the Belgian Spy fossils. *Am. J. Phys. Anthropol.* **2009**, *138*, 421–428. [CrossRef]